

See discussions, stats, and author profiles for this publication at: <https://www.researchgate.net/publication/230677659>

# Preparation of High-Quality Colloidal Mask for Nanosphere Lithography by a Combination of Air/Water Interface Self-Assembly and Solvent Vapor Annealing

ARTICLE *in* LANGMUIR · AUGUST 2012

Impact Factor: 4.46 · DOI: 10.1021/la3026182 · Source: PubMed

---

CITATIONS

16

---

READS

36

8 AUTHORS, INCLUDING:



**Xiaoqing Wang**

Chinese Academy of Sciences

54 PUBLICATIONS 537 CITATIONS

SEE PROFILE



**Qingfeng Yan**

Tsinghua University

104 PUBLICATIONS 988 CITATIONS

SEE PROFILE

# Preparation of High-Quality Colloidal Mask for Nanosphere Lithography by a Combination of Air/Water Interface Self-Assembly and Solvent Vapor Annealing

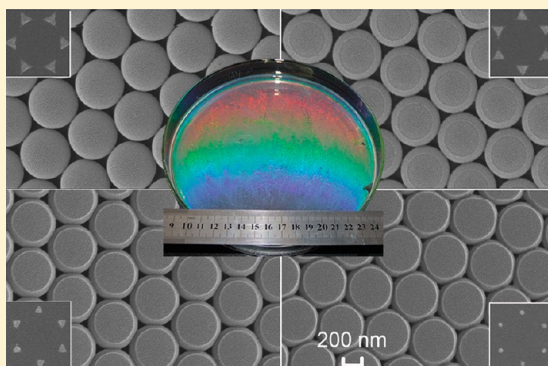
Jie Yu,<sup>†</sup> Chong Geng,<sup>†</sup> Lu Zheng,<sup>†</sup> Zhaohui Ma,<sup>‡</sup> Tianya Tan,<sup>‡</sup> Xiaoqing Wang,<sup>†</sup> Qingfeng Yan,<sup>\*,†</sup> and Dezhong Shen<sup>†</sup>

<sup>†</sup>Department of Chemistry, State Key Laboratory of New Ceramics and Fine Processing, Tsinghua University, Beijing 100084, China

<sup>‡</sup>Department of Physics, Liaoning University, Shenyang 110036, China

## S Supporting Information

**ABSTRACT:** Nanosphere lithography (NSL) has been regarded as an inexpensive, inherently parallel, high-throughput, materials-general approach to the fabrication of nanoparticle arrays. However, the order of the resulting nanoparticle array is essentially dependent on the quality of the colloidal monolayer mask. Furthermore, the lateral feature size of the nanoparticles created using NSL is coupled with the diameter of the colloidal spheres, which makes it inconvenient for studying the size-dependent properties of nanoparticles. In this work, we demonstrate a facile approach to the fabrication of a large-area, transferrable, high-quality latex colloidal mask for nanosphere lithography. The approach is based on a combination of the air/water interface self-assembly method and the solvent-vapor-annealing technique. It enables the fabrication of colloidal masks with a higher crystalline integrity compared to those produced by other strategies. By manipulating the diameter of the colloidal spheres and precisely tuning the solvent-vapor-annealing process, flexible control of the size, shape, and spacing of the interstice in a colloidal mask can be realized, which may facilitate the broad use of NSL in studying the size-, shape-, and period-dependent optical, magnetic, electronic, and catalytic properties of nanomaterials.



## 1. INTRODUCTION

Recently engineered nanomaterials have attracted a great deal of attention and have been studied extensively because of their size- and shape-dependent physical–chemical, optical, and magnetic properties for applications in various technologically important areas. Nanosphere lithography (NSL) has been recognized as an inexpensive, inherently parallel, high-throughput, and materials-general nanofabrication technique.<sup>1–10</sup> A typical NSL process starts from the self-assembly of a colloidal micro/nanosphere monolayer on a flat substrate. Subsequently, the colloidal sphere monolayer is used as a physical mask, and a material of choice is deposited onto the mask, thereby partially filling the interstices between the colloidal spheres. Finally, the colloidal sphere monolayer is removed by a lift-off process, and a periodic nanoparticle array of the deposited material is left on the substrate. The lattice spacing of the nanoparticle array can be controlled by changing the diameter of the colloidal spheres. The height of the individual nanoparticles is determined by the amount of material that is deposited through the mask. Typically, the shape of the nanoparticle is triangle-like and also dependent on the deposition technique used.<sup>11–14</sup> What makes the NSL technique appealing is that the lateral feature size of the resulting nanoparticles is approximately one-fifth the diameter

of the colloidal spheres.<sup>2,3</sup> Hence, the technique has been extensively used to fabricate well-ordered 2D periodic arrays of nanoparticles and investigate their size-dependent electrochemical, thermodynamic, catalytic, optical, and magnetic properties.

So far, there have been two main restrictions that have hindered wide applications of NSL in the fabrication of high-quality nanoparticle arrays. First, the order of the resulting nanoparticle array is essentially dependent on the quality of the deposition mask (i.e., the colloidal monolayer). In most cases, a colloidal monolayer is formed on a solid substrate via convection-driven evaporative self-assembly techniques in a liquid medium. Although the colloidal monolayer may hold a high-quality crystalline structure with a monocrystalline domain size of up to a few hundred micrometers when it is in a wet state on the solid substrate, irregular cracks appear after the liquid is eventually evaporated. The formation of these extra cracks is attributable to the lateral shrinkage of the colloidal spheres with respect to the solid support substrate during the drying process.<sup>15–17</sup> These cracks will eventually deteriorate the

Received: June 29, 2012

Revised: July 20, 2012

order of the resulted nanoparticle array. Second, the size of interstices in a hexagonally close-packed colloidal monolayer is determined by the diameter of the colloidal spheres. Thus, the lateral feature size of the nanoparticles created using NSL is coupled with the diameter of the colloidal spheres.<sup>2,3</sup> This kind of coupling, however, results in a constraint to studying the size-dependent properties of nanoparticles when colloidal spheres with various diameters are not available.

To produce dried colloidal crystals with fewer or even no cracks, several research groups have tried to stick the colloidal spheres together before they shrink. For example, Ruhl and co-workers have reported the fabrication of colloidal crystals using core-shell spheres, of which the soft shell deforms and fills the interstices, preventing the generation of cracks.<sup>18</sup> Subsequently, Wang et al. synthesized latex particles with a hard polystyrene (PS) core and a soft poly(methyl methacrylate)/poly(acrylic acid) (PMMA/PAA) shell, from which crack-free and mechanical-strength-enhanced colloidal films were fabricated.<sup>19</sup> Kanai et al. have developed a gel-immobilization approach to producing dried colloidal crystals without cracks.<sup>20</sup> A loosely packed colloidal crystal was first immobilized in a hydrogel and then homogeneously shrunk by repetitive soaking in an aqueous solution with increasing concentration of ethanol, resulting in a dried film of densely packed colloidal crystal without cracks. Recently, Zhao and co-workers reported the fabrication of crack-free colloidal crystals by using a modified vertical deposition method.<sup>21,22</sup> In this method, a colloidal suspension of silica spheres containing a silica precursor was used in the vertical deposition. The hydrolysis of the silica precursor produced a silica sol-gel that filled up the voids between the self-assembled silica spheres to avoid the formation of cracks upon drying of the colloidal crystal film. However, these methods have been limited to 3D colloidal crystals. The feasibility of these presticking strategies in fabricating dried colloidal monolayers with minimized cracks is unknown. Considering that the generation of cracks mainly results from the lateral shrinkage of the colloidal spheres with respect to the solid support substrate, liquids such as gallium and mercury have been used as soft substrates in studying colloidal crystallization.<sup>23,24</sup> As expected, crystallization on a liquid surface eliminated the problem of lateral sticking of colloidal spheres to the solid support substrate during the drying process, resulting in dried colloidal crystals with a lower defect density and fewer cracks. However, it is difficult to transfer the as-formed colloidal crystal without disturbing its crystalline integrity from these toxic liquid surfaces to other substrates. The crystallization of colloidal spheres at the air/water interface has been proven to be able to produce large-area, high-quality colloidal monolayers.<sup>10,25–28</sup> When applied to NSL, these colloidal monolayers need to be transferred onto a desired solid substrate. Still, they will experience the drying process and suffer the formation of extra cracks, causing a deterioration in the quality of the colloidal mask for NSL.

Control over the size of interstices in a colloidal mask is of paramount importance to studying the size-dependent properties of nanoparticles created by NSL. Although the interstice size in an as-formed colloidal monolayer is coupled to the diameter of the colloidal spheres, the intentional deformation of colloidal spheres after crystallization may result in a colloidal mask with tunable interstice size, thus enabling the manipulation of nanoparticle sizes. In previous work, thermal annealing at a temperature above the glass-transition temperature of the latex colloidal spheres has been applied to produce

a colloidal monolayer with controllable interstice size.<sup>29,30</sup> Also, a combination of solvent swelling and microwave annealing has been used to shrink the interstice size in a colloidal monolayer.<sup>31</sup> Recently, Vossen et al. have used ion bombardment to control the interstice size in colloidal masks.<sup>32</sup> However, the methods mentioned above are all based on the post-treatment of a colloidal monolayer that has already been deposited on a solid substrate. During the deformation of colloidal spheres by thermal annealing, solvent swelling, or ion bombardment, extra cracks will inevitably be induced because the colloidal spheres stick to the solid support substrate. Ozin's group and van Blaaderen's group have reported an alternative approach to decreasing the interstice size in a colloidal monolayer by the chemical vapor deposition (CVD) of silica.<sup>33,34</sup> The process allows a decrease in the interstice size homogeneously and linearly. Another advantage of this approach is that no extra cracks will be generated in the colloidal mask because the CVD coating does not involve the deformation of colloidal spheres. Nevertheless, silica will also deposit on the substrate through the interstice during CVD coating, which makes it unsuitable for NSL application.

In this work, we demonstrate an approach to the fabrication of high-quality colloidal mask for NSL application. The process flow is schematically illustrated in Figure 1. A latex colloidal

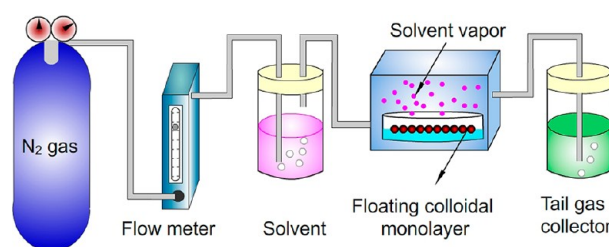


**Figure 1.** Schematic illustration of the fabrication of high-quality colloidal masks for NSL.

monolayer was first grown via the air/water interface self-assembly method.<sup>26–28</sup> Solvent vapor annealing was applied to treat the as-formed colloidal monolayer floating on the water surface, which was then transferred onto a desired solid substrate as a deposition mask for NSL. Such a colloidal mask presents several prominent advantages compared to those obtained by other methods. First, large-area (up to 6 in. wafers) colloidal monolayers can be fabricated rapidly by self-assembling colloidal spheres at the air/water interface rather than on a solid substrate. Second, the interstice size of the colloidal mask can be precisely controlled by manipulating the solvent-vapor-annealing process. Third, the tensile stress due to the deformation of colloidal spheres during solvent vapor annealing could be released through the underneath smooth, soft liquid surface. Accordingly, extra cracks arising from the constraint of sphere deformation on a rigid substrate were eliminated. Fourth, the mechanical strength of the colloidal mask was enhanced because the latex spheres were fused together upon solvent vapor annealing. As a result, extra cracks induced by the evaporation of water could be reduced to a maximum degree when the colloidal mask was transferred to a desired solid substrate for NSL. Finally, the colloidal mask could be transferred to any kind of substrate, including rigid, flexible, flat, or curved solid substrates. These advantages make the approach presented here very appealing for the fabrication of high-quality colloidal masks for NSL. The effects of the

solvent type, amount of solvent vapor, and annealing time on tuning the interstice size in a colloidal mask were systematically studied. The mechanism of colloidal sphere deformation during solvent vapor annealing was investigated. Silver nanoparticle arrays with various sizes and periods were produced using the high-quality colloidal masks fabricated by the approach described above.

## 2. EXPERIMENTAL SECTION

**Synthesis of PS Spheres and Preparation of Colloidal Monolayers.** Monodisperse PS colloidal spheres of 400, 598, 658, and 887 nm diameter with a polydispersity of less than 3% were synthesized by using the emulsifier-free polymerization method.<sup>35</sup> The PS spheres were washed with DI water three times by repeated centrifugation and finally dispersed in water diluted with an equal volume of ethanol. Microscopic glass slides with a thickness of 1 mm were cut into pieces. The glass pieces were cleaned by successive sonication in acetone, ethanol, and deionized (DI) water. Then they were ultrasonicated in piranha solution containing concentrated sulfuric acid (95–98%, Sinopharm Chemical Reagent Beijing Co., Ltd.) and hydrogen peroxide (30%, Sinopharm Chemical Reagent Beijing Co., Ltd.) (3:1 v/v H<sub>2</sub>SO<sub>4</sub>/H<sub>2</sub>O<sub>2</sub>) for 30 min. After being washed with a copious amount of DI water, they were dried in flow of nitrogen before use. For the self-assembly of PS colloidal spheres on the air/water interface, a piece of cleaned glass slide was first placed in the center of a glass Petri dish with a diameter of 9 cm. DI water was then carefully added to the dish with its surface at the same level as the upper edge of the cleaned horizontal glass slide. Ten ~20  $\mu$ L portions of a colloidal water/ethanol suspension with a volume fraction of 1.5% were dropped and spread freely on the glass slide. Once the suspension contacted the surrounding DI water at the edges of the glass slide, it was observed that the PS spheres spread on the water surface rapidly and assembled into 2D arrays in several seconds. To consolidate the colloidal arrays, a drop of 1 wt % sodium dodecyl sulfate (SDS, Sinopharm Chemical Reagent Beijing Co., Ltd.) solution was added to reduce the water surface tension. Iridescent color was observed immediately after the addition of SDS surfactant, indicating the formation of highly ordered colloidal monolayer at the air/water interface. The area of the colloidal monolayer obtained depended on the amount of colloidal suspension dropped on the glass slide and the size of the glass Petri dish.

**Solvent Vapor Annealing of the Floating PS Colloidal Monolayer.** The glass Petri dish with a floating PS colloidal monolayer was carefully transferred to a sealed glass vessel with two gas outlets. Organic solvent vapor was carried into the glass vessel through a gas outlet by nitrogen gas using a bubbling system as shown in Figure 1. The glass vessel has dimensions of 14.5 cm  $\times$  14.5 cm  $\times$  7.5 cm. Through another gas outlet, the extra solvent vapor was absorbed by a tail gas collection system. The amount of solvent vapor inside the glass vessel thus was controlled by the flow rate of the nitrogen carrier gas. After a desired annealing time, the glass cover was opened and the annealed colloidal monolayer was ready to be transferred to a solid substrate.

**Transferring the Annealed Colloidal Monolayer to a Solid Substrate.** To transfer the solvent-vapor-annealed colloidal monolayer to a solid substrate easily, the liquid level in the Petri dish was raised by adding more DI water. Various solid substrates such as glass, silicon wafer, a sapphire substrate, and a flexible plastic sheet were inserted beneath the annealed colloidal monolayer. The monolayer was then lifted off from the water surface as a whole and dried at room temperature.

**Fabrication of Silver Nanoparticle Arrays.** A layer of 50 nm Ag was deposited on the annealed colloidal monolayer on a silicon substrate by using an electronic beam evaporator (Denton Explorer 14) with a deposition rate of 0.2  $\text{\AA}/\text{s}$ . After deposition, the PS colloidal mask was removed from the substrate by sonication in toluene.

**Characterization.** Field-emission scanning electron microscope (FESEM) images were captured with a Gemini LEO 1530 instrument. The photographs of the PS colloidal monolayer floating on the water

surface and those deposited on different solid substrates were acquired using a digital camera (Fujifilm S205). The optical microphotographs of the PS colloidal monolayers were taken using an optical microscope (Olympus, BX51TRF) that was connected to a CCD camera (Pixelink-B742) and a computer for real-time image recording. Atomic force micrographs (AFMs) were recorded on a Nanoscope III Multimode SPM (Digital Instruments) with an AS-12 ("E") scanner operated in tapping mode.

## 3. RESULTS AND DISCUSSION

**Preparation of a Colloidal Monolayer by Air/Water Interface Assembly.** Among many techniques used to fabricate colloidal monolayers, self-assembly at the air/water interface has been proven to be a facile and efficient approach to large-area colloidal monolayers because nanospheres at the interface are able to form an exclusively single layer without variation in the layer thickness, which can hardly be realized in the evaporation-induced self-assembly on solid substrates.<sup>10,25–28</sup> Latex spheres are the most favorable building blocks for the self-assembly of colloidal monolayers for NSL application because they can be readily synthesized or are commercially available as monodisperse spheres with controllable diameters. For the fabrication of colloidal monolayers for NSL, PS latex spheres with diameters of 400, 598, 658, and 887 nm were synthesized via emulsifier-free polymerization.<sup>35</sup> In principle, there are no limits on the area of the colloidal monolayer fabricated; it depends only on the dimensions of the glass Petri dish used in the air/water interface self-assembly process. A colloidal monolayer with an area of up to several tens of  $\text{cm}^2$  could be obtained in a few minutes. Figure S1 in the Supporting Information shows a PS monolayer floating on the water surface in a Petri dish with a diameter of 15.5 cm. Iridescent color was observed immediately after the self-assembly of colloidal spheres, indicating the formation of a highly ordered colloidal monolayer at the air/water interface.

**Annealing the Floating Colloidal Monolayer with Different Solvent Vapors.** The interstice size between PS colloidal spheres diminishes upon annealing with organic solvent vapor. This happens through the interaction of polymer chains between neighboring PS colloidal spheres, which is similar to what occurs during thermal annealing. Under thermal annealing at a temperature above the glass-transition temperature of PS, the interaction between PS chains is enhanced by higher-thermal-energy-induced Brownian motion. As a consequence, polymer chains will intermix, and neighboring PS spheres tend to fuse together, leading to the interstice size shrinking. However, it is by the improved mobility of the polymer chains that the interaction is enhanced in the case of solvent vapor annealing. In the presence of a good organic solvent vapor, PS colloidal spheres will absorb the solvent molecules from the vapor. The spheres exposed to the solvent vapor become soft because polymer chains in the sphere prefer to adhere to the solvent molecules rather than to each other. This in turn allows spheres to exchange molecules over contact areas with neighboring spheres. Unfavorable large surface energies of spheres are thus minimized, leading to a decrease in interstice size in the floating PS colloidal monolayer.<sup>36</sup> The mobility of polymer chains will be determined by the type of organic solvent vapors; therefore, the shrinking rate of interstice size is believed to be related to the type of solvent used.

Two common volatile organic solvents, tetrahydrofuran (THF) and toluene, were utilized to anneal the floating colloidal monolayer. As schematically shown in Figure 1, the



glass Petri dish with a colloidal monolayer floating at the air/water interface was settled in a sealed glass chamber. The vapor of a good solvent for PS colloids, THF or toluene, was introduced into the chamber through a gas-bubbling system. The amount of solvent vapor applied to the colloidal monolayer was controlled by the flow rate of nitrogen ( $N_2$ ) carrier gas. Scanning electron microscope (SEM) images in Figure 2 show the 598 nm PS colloidal monolayers after

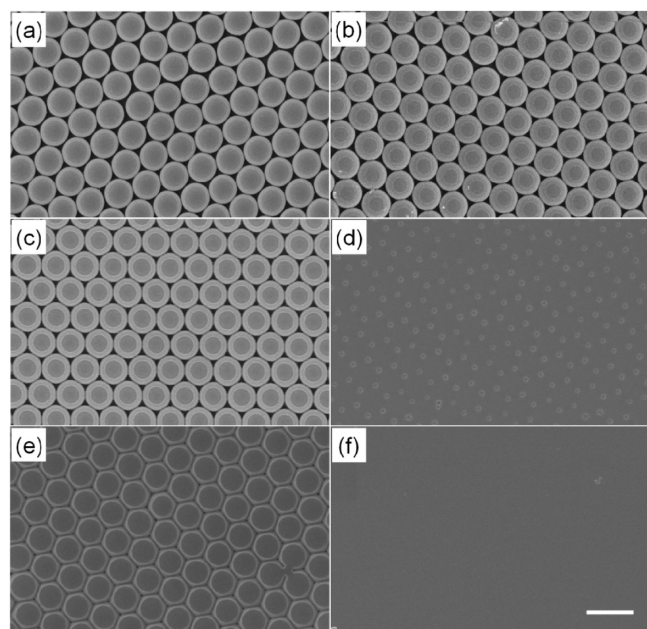


**Figure 2.** PS colloidal monolayers annealed with different solvent vapors. THF was used in a, c, and e, and toluene was used in b, d, and f. The flow rates of  $N_2$  carrier gas in a and b, c and d, e and f were 25, 50, and 100 mL/min, respectively. The annealing times in a and b, c and d, and e and f were 2, 1, and 0.5 h, respectively. The original PS sphere diameter is 598 nm. The scale bar is 1  $\mu$ m.

annealing in THF and toluene under identical annealing conditions. The flow rates of  $N_2$  carrier gas in a and b, c and d, e and f were 25, 50, and 100 mL/min, respectively. The annealing times in a and b, c and d, and e and f were 2, 1, and 0.5 h, respectively. It is obviously seen that the interstice size shrank much more for colloidal monolayers annealed in toluene than for that in THF vapor under otherwise identical annealing conditions. At room temperature, the saturated vapor pressure of toluene is lower than that of THF. The amount of THF vapor in the annealing chamber should be more than that of toluene vapor when the flow rate of nitrogen carrier gas is identical. On the contrary, the degree of annealing of the floating PS colloidal monolayer was higher in toluene vapor than in THF vapor. This implies that the mobility of PS chains was improved more in the presence of toluene than in the case of THF. The different mobility of polymer chains in various solvent vapors can be interpreted by the solubility parameter difference. In general, materials with similar solubility parameters will be able to interact with each other, resulting in swelling, miscibility, or solvation. When the difference in solubility parameters between the polymer and solvent is larger than  $3.5 \text{ J}^{1/2} \text{ cm}^{-3/2}$ , swelling and solvation could not occur. PS has a solubility parameter ranging from 17.8 to  $18.6 \text{ J}^{1/2} \text{ cm}^{-3/2}$  depending on its molecular weight.<sup>37</sup> The solubility parameters of toluene and THF are  $18.2$  and  $20.2 \text{ J}^{1/2} \text{ cm}^{-3/2}$ , respectively.

Therefore, toluene is likely to be a better solvent for PS spheres compared to THF because its solubility parameter is closer to that of PS. PS chains are believed to possess higher mobility in the presence of toluene vapor than in THF vapor. As a consequence, stronger interactions between PS chains resulted during toluene vapor annealing, leading to a faster shrinking of the interstice size. The solubility parameter of ethanol is  $26.2 \text{ J}^{1/2} \text{ cm}^{-3/2}$ , which is much larger than that of PS spheres. As expected, the PS colloidal monolayer annealed in ethanol vapor showed a negligible change in interstice size (data not shown).

The above experimental results have indicated that the interstice size decreased too fast when toluene vapor was adopted to anneal the floating PS colloidal monolayer. In contrast, THF seemed to be able to provide a mild solvent vapor for annealing PS colloidal monolayer. Thus, THF was used to manipulate the interstice size of a PS colloidal monolayer during solvent vapor annealing in the following sections.

**Manipulating the Interstice Size in a Colloidal Mask via the Flow Rate Control of Carrier Gas.** The change of interstice size in a 598 nm colloidal monolayer upon THF vapor annealing by using different flow rates of nitrogen carrier gas is shown in Figure 3. Given a fixed annealing time of 60

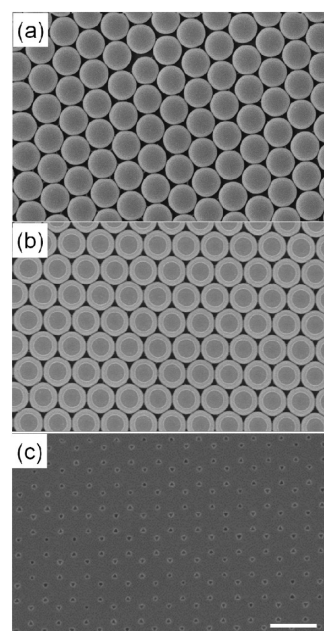


**Figure 3.** PS colloidal monolayers after THF vapor annealing with different flow rates of  $N_2$  carrier gas: (a) 25, (b) 50, and (c) 100 mL/min. The original PS sphere diameter is 598 nm. The annealing time is 60 min. The scale bar is 1  $\mu$ m.

min, the higher the flow rate of the nitrogen carrier gas, the more the colloidal spheres deformed. As a result, the interstice size decreased with increasing flow rate of nitrogen carrier gas. The interstice size was defined as the shortest distance between the point in physical contact between two spheres and a point on the third sphere in a hexagonal close-packed colloidal monolayer. And the interstice spacing was defined as the distance between the centers of two neighboring interstice. Without THF vapor annealing, the interstice size was 140 nm, which was around the theoretical value of  $0.23D$ , where  $D$  is the diameter of the PS colloidal spheres. The interstice spacing was 340 nm, which was approximately equal to the theoretical value

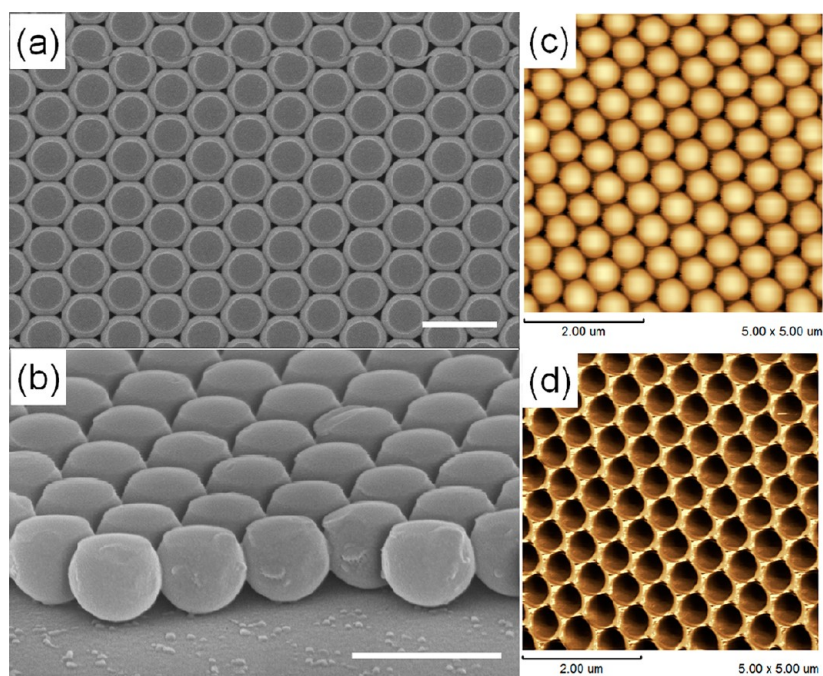


**Figure 4.** (a) Top and (b) tilted cross-sectional views of a PS colloidal monolayer with THF vapor annealing for 10 min. The original PS sphere diameter is 598 nm. The flow rate of the nitrogen carrier gas is 100 mL/min. The scale bars in a and b are 1  $\mu\text{m}$ . The AFM surface topography image and phase image of the annealed PS colloidal monolayer are shown in c and d, respectively.

of  $0.57D$ . When nitrogen gas with a flow rate of 25 mL/min was adopted to carry THF vapor into the chamber, the interstice size changed very little from 140 to 130 nm (Figure 3a). When the flow rate of nitrogen gas was increased to 50 mL/min, the interstice size decreased to 115 nm (Figure 3b). Further increasing the  $\text{N}_2$  flow rate to 100 mL/min resulted in an interstice with a nominal size of about 40 nm (Figure 3c). However, nanosphere lithography using the annealed colloidal monolayer shown in Figure 3c as a deposition mask resulted in no formation of nanoparticles array, which indicated that the interstice between PS spheres had actually been closed already. It was noticeable that the interstice spacing remained unchanged during solvent vapor annealing.

Besides the change in interstice size, a dramatic morphology change in the colloidal crystal was that a special region emerged on top of each PS sphere after solvent vapor annealing. The special region appeared dark gray, as shown in SEM images in both Figures 2 and 3. It was obvious that the area of the special region increased with increased solvent vapor exposure. To investigate the morphology of the annealed colloidal spheres further, enlarged top and tilted cross-sectional views of a PS monolayer annealed by using THF for 10 min with a  $\text{N}_2$  flow rate of 100 mL/min were presented in Figure 4a,b, respectively. It was clearly seen from the tilted cross-sectional view that the top part of the PS spheres was flattened whereas the bottom part remained the original spherical shape after solvent vapor annealing. The flattened part corresponded to the dark-gray area in the top-view image shown in Figure 4a. In a floating colloidal monolayer, each PS nanosphere was actually divided into two parts by the water surface. The upper part of the colloidal spheres protruded out of the water and was exposed to solvent vapor. The lower part of the colloidal spheres was immersed in water, which enabled the protection of the bottom part of colloidal spheres from solvent vapor attack. Thus, only the upper part of the PS spheres was available to absorb solvent

molecules during solvent vapor annealing. The absorption of solvent vapor caused the PS spheres to deform and adhere to each other, which resulted in a decrease in the interstice size. Besides, it was found that the solvent-vapor-annealed part of PS spheres exhibited a different color compared to that immersed in water after drying. The color contrast is likely due to two reasons. One reason lies in the fact that the top part of the PS spheres has been flattened. During the flattening process, PS chains entangled again, which might result in a more densely packed PS network. The other possible reason lies in the fact that the material composition of the top part of the PS spheres has changed and might contain solvent molecules. To clarify this point, PS monolayers annealed with THF vapor were dried under vacuum for 24 h at 60  $^{\circ}\text{C}$  to remove THF completely. The SEM images of the annealed PS monolayer before and after vacuum drying are presented in Figure S2 in the Supporting Information. No obvious change in the morphology of the annealed PS monolayers was observed. The dark-gray color still existed after vacuum drying, which indicated that the color contrast probably resulted only from the dense entanglement of polymer chains in the top part of the PS spheres after annealing. The atomic force microscopy (AFM) surface topography image and phase image of the annealed PS colloidal monolayer are shown in Figure 4c,d, respectively. The dark color that appeared on the flattened area also implied that PS chains stacked more densely than those in other areas of the annealed spheres. Furthermore, the spherical shape was retained for the bottom part of PS spheres because of the water's protection against deformation. Compared to the colloidal monolayer annealed by traditional thermal annealing or ion beam exposure, the solvent-vapor-annealed colloidal monolayer floating on the water surface exhibited a distinctive morphology, which was a direct result of the partial annealing strategy used in this method.



**Tuning the Interstice Size between Colloidal Spheres via the Annealing Time.** The interstice size between colloidal spheres could also be accurately controlled through manipulating the annealing time. Figure 5 shows SEM images of a PS

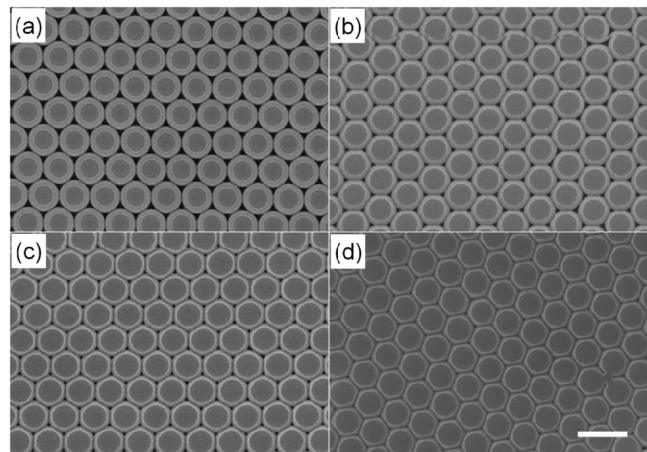


**Figure 5.** PS colloidal monolayers with different THF vapor annealing times. The original PS sphere diameter is 598 nm. The flow rate of the nitrogen carrier gas is 100 mL/min. The annealing times are 5, 10, 20, and 30 min in a–d, respectively. The scale bar is 1  $\mu$ m.

colloidal monolayer after THF vapor annealing with different time durations. The nitrogen flow rate was kept at 100 mL/min, which ensured the amount of THF vapor in the chamber to be fixed during annealing. The annealing times in Figure 5a–c were 5, 10, and 20 min, respectively. Accordingly, the corresponding interstice size in the colloidal monolayer decreased from the original 140 nm to 120, 89, and 47 nm, respectively. With the annealing time further increased to 30 min, the neighboring colloidal spheres were found to adhere completely with each other, and the interstices between colloidal spheres have almost disappeared. The interstice size as a function of the annealing time is plotted in Figure 6. It can

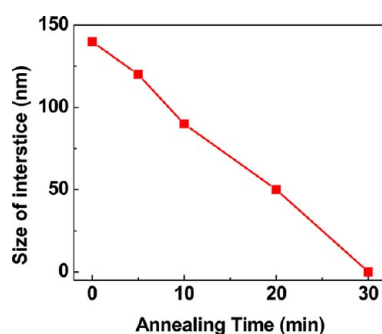


**Figure 6.** The interstice size as a function of the annealing time. The original PS sphere diameter was 598 nm. The flow rate of the nitrogen carrier gas was 100 mL/min.

be clearly seen that the size of the interstice decreases with the increase in the solvent annealing time, which gives an interstice size decreasing to a rate of around 10 nm/s. Therefore, one may acquire a colloidal mask with the desired interstice size by simply tuning the solvent-vapor-annealing time.

To demonstrate the facility of the solvent-vapor-annealing process, colloidal monolayers with PS spheres of other sizes were also tested. As an example, SEM images in Figure 7

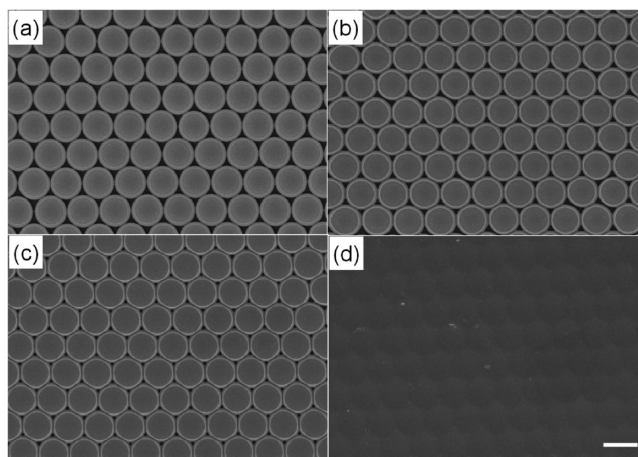


**Figure 7.** PS colloidal monolayers with different THF vapor annealing times. The original PS sphere diameter was 887 nm. The flow rate of the nitrogen carrier gas was 100 mL/min. The annealing times were 10, 15, 20, and 30 min in a–d, respectively. The scale bar is 1  $\mu$ m.

illustrate the change in the interstice size in a floating PS colloidal monolayer with a sphere size of 887 nm upon THF vapor annealing with different time durations. As expected, the shrinking of the interstice between PS spheres showed a similar trend to that observed in a 598 nm PS colloidal monolayer with increased annealing time. Meanwhile, similar results were obtained by annealing a floating 400 nm PS colloidal monolayer with THF vapor. Thus, it could be deduced that this solvent-vapor-annealing strategy can be applied to PS colloidal monolayers with various sphere sizes as long as they can be produced via the air/water interface self-assembly method.

**NSL by Using Solvent-Vapor-Annealed PS Colloidal Monolayers as Deposition Masks.** The PS colloidal monolayer annealed by solvent vapor at the air/water interface was proven to be a high-quality deposition mask for NSL. On the one hand, the interstice size in the deposition mask could be predefined and tuned by manipulating the sphere size and the annealing process. On the other hand, extra cracks due to colloidal sphere deformation as observed in the conventional thermal annealing and ion bombardment of PS colloidal monolayers as-formed on a solid substrate were eliminated. In addition, extra cracks arising from the evaporation of water during the drying of a self-assembled colloidal monolayer on a solid substrate were reduced to a large extent because the annealed PS colloidal spheres fused together and the colloidal monolayer had a higher mechanical strength. To track the evolution of crystalline integrity during the fabrication of colloidal masks for NSL, optical microscopy photographs were captured for a 658 nm PS colloidal monolayer before (sample A) and after (sample B) solvent vapor annealing as well as for the PS monolayer transferred onto a glass substrate after annealing and subsequently drying (sample C). As a reference, a dried PS colloidal monolayer was also prepared by transferring a floating PS monolayer free of solvent annealing onto a glass substrate (sample D). Then the dried PS colloidal monolayer prepared above was annealed by THF vapor under identical experimental conditions (sample E). From the optical microscopy images of these five samples, as shown in Figure S3 in the Supporting Information, one may compare the crystalline integrity of these PS colloidal monolayers. To evaluate the quality of the monolayers in a quantitative way, the densities of dislocations and cracks were calculated for each sample. Point

defects were not considered because they were mainly determined by the polydispersity of the colloidal spheres used. The densities of dislocations and cracks in these samples, calculated by dividing the length of defect lines in the photograph by its area, are presented in Figure 8. It is clearly

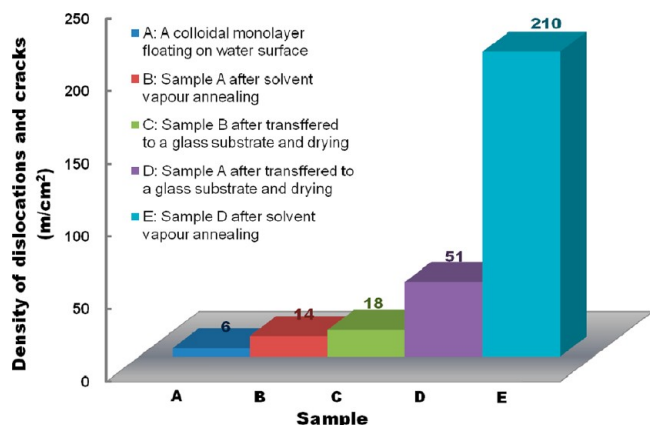


**Figure 8.** Density of dislocations and cracks in various fabricated colloidal masks. Sample A: an original PS colloidal monolayer self-assembled at the air/water interface. Sample B: an annealed PS monolayer floating on the water surface. Samples C: an annealed PS monolayer after drying on a glass substrate. Sample D: a dried colloidal monolayer prepared by transferring the floating PS monolayer onto a glass substrate. Sample E: sample D after solvent vapor annealing.

seen that both the annealed PS monolayer floating on the water surface (sample B) and its dry descendant on the glass substrate (sample C) inherit the good crystalline integrity of the original PS colloidal monolayer self-assembled at the air/water interface (sample A). The density of dislocations and cracks in samples A–C is of the same order of magnitude, which is below 20 m/cm<sup>2</sup>. However, the dried colloidal monolayer obtained by transferring the floating PS monolayer to a glass substrate (sample D) shows inferior crystalline integrity with a defect density larger than 50 m/cm<sup>2</sup>. THF vapor annealing of sample D results in a colloidal monolayer with further deteriorated quality (sample E) showing a defect density larger than 200 m/cm<sup>2</sup>, which is several tens of times higher than that in sample A. These results indicate that the solvent vapor annealing of a PS colloidal monolayer self-assembled at the air/water interface may provide high-quality colloidal masks with a tunable interstice size.

Furthermore, the high-quality PS colloidal monolayer annealed by solvent vapor could be transferred to any desired substrate as a deposition mask for NSL. Optical microphotographs shown in Figure S4 in the Supporting Information present THF-vapor-annealed 658 nm PS colloidal monolayers that were deposited on a 2 in. sapphire substrate, a 4 in. silicon wafer, and a flexible plastic substrate, respectively. The deposition of an annealed PS monolayer on other rigid or flexible, hydrophilic or hydrophobic, or flat or curved solid substrates is also possible. As expected, the crystalline integrity of the PS monolayer is well maintained after transferring and drying on the solid substrates. The transfer of an annealed colloidal monolayer with defined interstice size onto a desired substrate without disturbing its crystalline integrity is of paramount importance for the fabrication of nanoparticle arrays on various substrates by means of NSL.

For demonstration purposes, Ag nanoparticle arrays were fabricated on silicon substrates by using annealed PS colloidal crystals as deposition masks. The SEM images in Figure 9 are

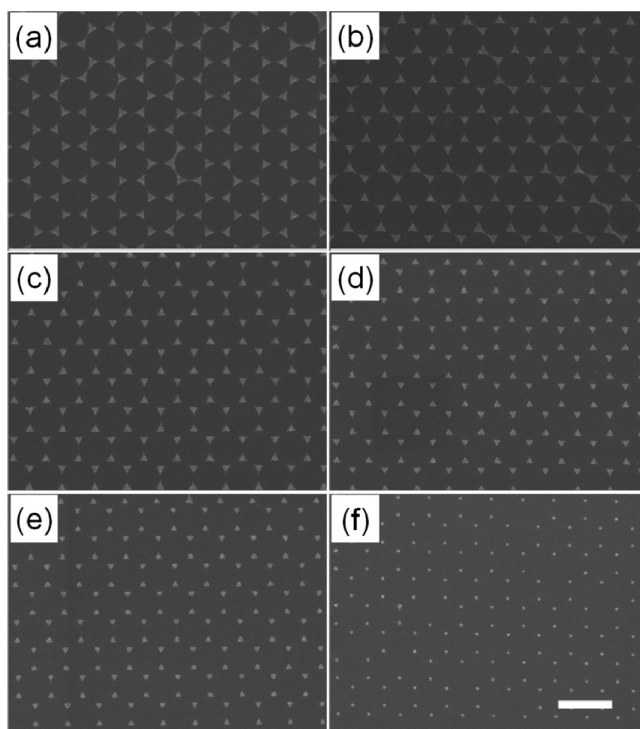


**Figure 9.** Ag nanoparticle arrays produced using 598 nm PS colloidal masks with (a) no THF vapor annealing and (b–f) prolonged annealing time. The feature sizes of Ag nanoparticles are 140, 119, 102, 93, 80, and 53 nm in a–f, respectively. The scale bar is 1  $\mu$ m.

Ag nanoparticle arrays produced using 598 nm PS colloidal masks with no THF vapor annealing (Figure 9a) and prolonged annealing times (45, 60, 70, 80, and 88 min corresponding to Figure 9b–f, respectively). These colloidal masks are shown in Figure S5 in the Supporting Information. As expected, the Ag nanoparticles obtained possess a honeycomb lattice resulting from the close-packed PS colloidal spheres. With the annealing time increasing, the interstice size decreased gradually. In addition, the shape of the interstice also changed from quasi-triangular to distorted circular (Figure S5, Supporting Information). Consequently, Ag nanoparticles show a similar change in size and shape, as observed in Figure 9. When the interstice closed because of too long an annealing time, no Ag nanoparticle array was obtained.

Solvent vapor annealing reduces the interstice size in a colloidal mask. Thus, the interstice size is uncoupled from the diameter of the colloidal spheres as well as the interstice spacing. It is now, for example, possible to obtain metal nanoparticles of the same size but with different interparticle spacing. SEM images in Figure 10 show three PS colloidal masks obtained by THF vapor annealing of 400, 598, and 887 nm PS colloidal monolayers. The interstice size in these colloidal masks has been tuned to be nearly the same (i.e., 90 nm) by precisely manipulating the solvent-vapor-annealing parameters. As a result, Ag nanoparticle arrays fabricated by using these colloidal masks exhibit a similar feature size but a different period. The simultaneous tuning of nanoparticle size and interparticle spacing enables one to study the size- and



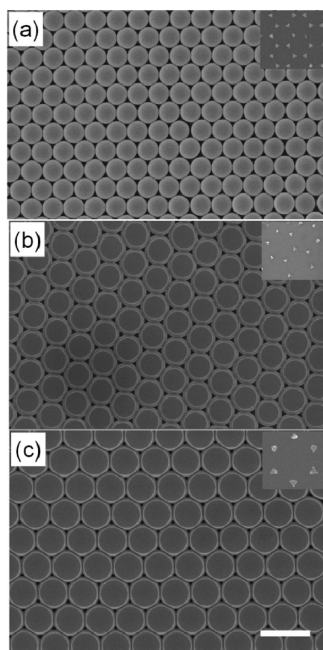


**Figure 10.** PS colloidal masks obtained by THF vapor annealing of (a) 400, (b) 598, and (c) 887 nm PS colloidal monolayers. Ag nanoparticle arrays (the insets) resulted from these colloidal masks possess nearly the same feature size but different periods. The scale bar is 1  $\mu\text{m}$ .

period-dependent optical, magnetic, electronic, and catalytic properties of nanoparticle arrays.

#### 4. CONCLUSIONS

We have developed a facile approach to the fabrication of large-area, transferrable, high-quality latex colloidal masks for nanosphere lithography. The approach is based on a combination of the air/water interface self-assembly method and the solvent-vapor-annealing technique. It enables the fabrication of colloidal masks with a higher crystalline integrity compared to those produced by other strategies. Extra cracks and dislocations that appear in colloidal masks fabricated by using conventional methods are eliminated to a large degree. By manipulating the diameter of the colloidal spheres and precisely tuning the solvent-vapor-annealing process, flexible control over the size, shape, and spacing of the interstice in a colloidal mask can be realized, which may facilitate the broad use of NSL to study the size-, shape-, and period-dependent optical, magnetic, electronic, and catalytic properties of nanomaterials. Although only highly ordered metallic nanoparticle arrays have been fabricated by using the colloidal masks in this study, we envision that it is possible to produce nanoparticle arrays of other functional materials with a desired feature size, shape, and period on a rigid or flexible, flat or curved, or hydrophilic or hydrophobic solid substrate by using a similar strategy. Ultimately, these nanoparticle arrays may find great potential applications in many important areas, such as plasmonics,<sup>3,38</sup> surface-enhanced Raman scattering (SERS),<sup>39,40</sup> biological and chemical sensing,<sup>41,42</sup> nanoimprinting,<sup>43</sup> magnetics,<sup>44,45</sup> field emission,<sup>30</sup> and other biological and electronic applications.<sup>46</sup>

#### ■ ASSOCIATED CONTENT

##### Supporting Information

Optical photograph of a floating PS colloidal monolayer with a large area fabricated by the air/water interface self-assembly method. Optical microphotographs of five different PS colloidal monolayers mentioned in the main text. Optical photographs of annealed PS colloidal monolayers that were transferred to different substrates. SEM images of a THF-vapor-annealed 598 nm PS colloidal monolayer before and after vacuum drying. SEM images of 598 nm PS colloidal monolayers with different THF vapor annealing times. This material is available free of charge via the Internet at <http://pubs.acs.org>.

#### ■ AUTHOR INFORMATION

##### Corresponding Author

\*E-mail: [yanqf@mail.tsinghua.edu.cn](mailto:yanqf@mail.tsinghua.edu.cn).

##### Notes

The authors declare no competing financial interest.

#### ■ ACKNOWLEDGMENTS

This work was supported by the Natural Science Foundation of China (project nos. 50903046 and 51173097), the Fok Ying Tung Education Foundation (project no. 122018), the Research Fund for the Doctoral Program of Higher Education of China (project no. 20090002120043), and the Tsinghua University Initiative Scientific Research Program.

#### ■ REFERENCES

- (1) Deckman, H. W.; Dunsmuir, J. H. Natural lithography. *Appl. Phys. Lett.* **1982**, *41*, 377–379.
- (2) Hulstee, J. C.; Van Duyn, R. P. Nanosphere lithography: a materials general fabrication process for periodic particle array surfaces. *J. Vac. Sci. Technol., A* **1995**, *13*, 1553–1558.
- (3) Haynes, C. L.; Van Duyn, R. P. Nanosphere lithography: a versatile nanofabrication tool for studies of size-dependent nanoparticle optics. *J. Phys. Chem. B* **2001**, *105*, 5599–5611.
- (4) Yang, S. M.; Jang, S. G.; Choi, D. G.; Kim, S.; Yu, H. K. Nanomachining by colloidal lithography. *Small* **2006**, *2*, 458–475.
- (5) Zhang, G.; Wang, D. Colloidal lithography—the art of nanochemical patterning. *Chem.—Asian J.* **2009**, *4*, 236–245.
- (6) Zhang, J.; Li, Y.; Zhang, X.; Yang, B. Colloidal self-assembly meets nanofabrication: from two-dimensional colloidal crystals to nanostructure arrays. *Adv. Mater.* **2010**, *22*, 4249–4269.
- (7) Yang, S.; Lei, Y. Recent progress on surface pattern fabrications based on monolayer colloidal crystal templates and related applications. *Nanoscale* **2011**, *3*, 2768–2782.
- (8) Li, Y.; Koshizaki, N.; Cai, W. Periodic one-dimensional nanostructured arrays based on colloidal templates, applications, and devices. *Coord. Chem. Rev.* **2011**, *255*, 357–373.
- (9) Li, L.; Zhai, T.; Zeng, H.; Fang, X.; Bando, Y.; Golberg, D. Polystyrene sphere-assisted one-dimensional nanostructure arrays: synthesis and applications. *J. Mater. Chem.* **2011**, *21*, 40–56.
- (10) Ye, X.; Qi, L. Two-dimensionally patterned nanostructures based on monolayer colloidal crystals: controllable fabrication, assembly, and applications. *Nano Today* **2011**, *6*, 608–631.
- (11) Kosior, A.; Kandulski, W.; Chudzinski, P.; Kempa, K.; Giersig, M. Shadow nanosphere lithography: simulation and experiment. *Nano Lett.* **2004**, *4*, 1359–1363.
- (12) Gwinner, M. C.; Koroknay, E.; Fu, L. W.; Patoka, P.; Kandulski, W.; Giersig, M.; Giessen, H. Periodic large-area metallic split-ring resonator metamaterial fabrication based on shadow nanosphere lithography. *Small* **2009**, *5*, 400–406.
- (13) Retsch, M.; Tamm, M.; Bocchio, N.; Horn, N.; Forch, R.; Jonas, U.; Kreiter, M. Parallel preparation of densely packed arrays of 150-nm

- gold-nanocrescent resonators in three dimensions. *Small* **2009**, *5*, 2105–2110.
- (14) Ye, S.; Routzahn, A. L.; Carroll, R. L. Fabrication of 3D metal dot arrays by geometrically structured dynamic shadowing lithography. *Langmuir* **2011**, *27*, 13806–13812.
- (15) Teh, L. K.; Tan, N. K.; Wong, C. C.; Li, S. Growth imperfections in three-dimensional colloidal self-assembly. *Appl. Phys. A: Mater. Sci. Process.* **2005**, *81*, 1399–1404.
- (16) Singh, K. B.; Tirumkudulu, M. S. Cracking in drying colloidal films. *Phys. Rev. Lett.* **2007**, *98*, 218302.
- (17) Xu, P.; Mujumdar, A. S.; Yu, B. Drying-induced cracks in thin film fabricated from colloidal dispersions. *Drying Technol.* **2009**, *27*, 636–652.
- (18) Ruhl, T.; Spahn, P.; Hellmann, G. P. Artificial opals prepared by melt compression. *Polymer* **2003**, *44*, 7625–7634.
- (19) Wang, J.; Wen, Y.; Ge, H.; Sun, Z.; Zheng, Y.; Song, Y.; Jiang, L. Simple fabrication of full color colloidal crystal films with tough mechanical strength. *Macromol. Chem. Phys.* **2006**, *207*, 596–604.
- (20) Kanai, T.; Sawada, T. New route to produce dry colloidal crystals without cracks. *Langmuir* **2009**, *25*, 13315–13317.
- (21) Wang, L.; Zhao, X. S. Fabrication of crack-free colloidal crystals using a modified vertical deposition method. *J. Phys. Chem. C* **2007**, *111*, 8538–8542.
- (22) Cai, Z.; Teng, J.; Xia, D.; Zhao, X. S. Self-assembly of crack-free silica colloidal crystals on patterned silicon substrates. *J. Phys. Chem. C* **2011**, *115*, 9970–9976.
- (23) Griesebock, B.; Egen, M.; Zentel, R. Large photonic films by crystallization on fluid substrates. *Chem. Mater.* **2002**, *14*, 4023–4025.
- (24) Zhang, J.-T.; Wang, L.; Chao, X.; Asher, S. A. Periodicity-controlled two-dimensional crystalline colloidal arrays. *Langmuir* **2011**, *27*, 15230–15235.
- (25) Gu, Z.-Z.; Wang, D.; Möhlwald, H. Self-assembly of microspheres at the air/water/air interface into free-standing colloidal crystal films. *Soft Matter* **2007**, *3*, 68–70.
- (26) Li, C.; Hong, G.; Wang, P.; Yu, D.; Qi, L. Wet chemical approaches to patterned arrays of well-aligned ZnO nanopillars assisted by monolayer colloidal crystals. *Chem. Mater.* **2009**, *21*, 891–897.
- (27) Retsch, M.; Zhou, Z.; Rivera, S.; Kappl, M.; Zhao, X. S.; Jonas, U.; Li, Q. Fabrication of large-area, transferable colloidal monolayers utilizing self-assembly at the air/water interface. *Macromol. Chem. Phys.* **2009**, *210*, 230–241.
- (28) Moon, G. D.; Lee, T. I.; Kim, B.; Chae, G.; Kim, J.; Kim, S.; Myoung, J.-M.; Jeong, U. Assembled monolayers of hydrophilic particles on water surfaces. *ACS Nano* **2011**, *5*, 8600–8612.
- (29) Gates, B.; Park, S. H.; Xia, Y. N. Tuning the photonic bandgap properties of crystalline arrays of polystyrene beads by annealing at elevated temperatures. *Adv. Mater.* **2000**, *12*, 653–656.
- (30) Zeng, H.; Xu, X.; Bando, Y.; Gautam, U. K.; Zhai, T.; Fang, X.; Liu, B.; Golberg, D. Template deformation-tailored ZnO nanorod/nanowire arrays: full growth control and optimization of field-emission. *Adv. Funct. Mater.* **2009**, *19*, 3165–3172.
- (31) Kosiorek, A.; Kandulski, W.; Glaczynska, H.; Giersig, M. Fabrication of nanoscale rings, dots, and rods by combining shadow nanosphere lithography and annealed polystyrene nanosphere masks. *Small* **2005**, *1*, 439–444.
- (32) Vossen, D. L. J.; Fific, D.; Penninkhof, J.; van Dillen, T.; Polman, A.; van Blaaderen, A. Combined optical tweezers/ion beam technique to tune colloidal masks for nanolithography. *Nano Lett.* **2005**, *5*, 1175–1179.
- (33) Miguez, H.; Tetreault, N.; Hatton, B.; Yang, S. M.; Perovic, D.; Ozin, G. A. Mechanical stability enhancement by pore size and connectivity control in colloidal crystals by layer-by-layer growth of oxide. *Chem. Commun.* **2002**, 2736–2737.
- (34) Vossen, D. L. J.; Penninkhof, J. J.; van Blaaderen, A. Chemical modification of colloidal masks for nanolithography. *Langmuir* **2008**, *24*, 5967–5969.
- (35) Shim, S. E.; Cha, Y. J.; Byun, J. M.; Choe, S. Size control of polystyrene beads by multistage seeded emulsion polymerization. *J. Appl. Polym. Sci.* **1999**, *71*, 2259–2269.
- (36) Kandulski, W. Shadow Nanosphere Lithography. Ph.D. Dissertation, Bonn University, 2007.
- (37) Suh, K. W.; Clarke, D. H. Cohesive energy densities of polymers from turbidimetric titrations. *J. Polym. Sci., Part A-1* **1967**, *5*, 1671–1681.
- (38) Haynes, C. L.; Van Duyne, R. P. Plasmon-sampled surface-enhanced Raman excitation spectroscopy. *J. Phys. Chem. B* **2003**, *107*, 7426–7433.
- (39) Abdelsalam, M. E.; Bartlett, P. N.; Baumberg, J. J.; Cintra, S.; Kelf, T. A.; Russell, A. E. Electrochemical SERS at a structured gold surface. *Electrochem. Commun.* **2005**, *7*, 740–744.
- (40) Abdelsalam, M. E.; Mahajan, S.; Bartlett, P. N.; Baumberg, J. J.; Russell, A. E. SERS at structured palladium and platinum surfaces. *J. Am. Chem. Soc.* **2007**, *129*, 7399–7406.
- (41) Yonzon, C. R.; Jeoung, E.; Zou, S. L.; Schatz, G. C.; Mrksich, M.; Van Duyne, R. P. A comparative analysis of localized and propagating surface plasmon resonance sensors: the binding of concanavalin A to a monosaccharide functionalized self-assembled monolayer. *J. Am. Chem. Soc.* **2004**, *126*, 12669–12676.
- (42) Vogel, N.; Jung, M.; Bocchio, N. L.; Retsch, M.; Kreiter, M.; Köper, I. Reusable localized surface plasmon sensors based on ultrastable nanostructures. *Small* **2010**, *6*, 104–109.
- (43) Kuo, C.-W.; Shiu, J.-Y.; Cho, Y.-H.; Chen, P. Fabrication of large-area periodic nanopillar arrays for nanoimprint lithography using polymer colloid masks. *Adv. Mater.* **2003**, *15*, 1065–1068.
- (44) Zhukov, A. A.; Ghanem, M. A.; Goncharov, A. V.; Bartlett, P. N.; de Groot, P. A. J. Magnetic nano-scale dot arrays from double-templated electrodeposition. *J. Magn. Magn. Mater.* **2004**, *272*, E1369–E1371.
- (45) Rybczynski, J.; Ebels, U.; Giersig, M. Large-scale, 2D arrays of magnetic nanoparticles. *Colloids Surf., A* **2003**, *219*, 1–6.
- (46) Singh, G.; Griesser, H. J.; Bremmell, K.; Kingshott, P. Highly ordered nanometer-scale chemical and protein patterns by binary colloidal crystal lithography combined with plasma polymerization. *Adv. Funct. Mater.* **2011**, *21*, 540–546.